Heliyon 10 (2024) e29380

Contents lists available at ScienceDirect

Heliyon

journal homepage: www.cell.com/heliyon

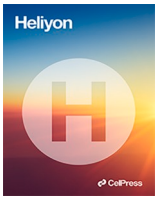

Research article

MHD free convection with Joule heating and entropy generation inside an *H*-shaped hollow structure

Md. Hasibul Islam, Riyan Hashem Jamy, Md. Shahneoug Shuvo, Sumon Saha *

Department of Mechanical Engineering, Bangladesh University of Engineering and Technology, Dhaka, 1000, Bangladesh

ARTICLE INFO

Keywords:
Magnetohydrodynamic
H-shaped structure
Free convection
Entropy generation
Joule heating

ABSTRACT

In this research, a free convective flow of water inside an *H*-shaped hollow structure which is subjected to the existence of an exterior magnetic field and Joule heating is computationally investigated. The structure's right and left upright surfaces are maintained at invariant ambient thermal condition, while the top and bottom-most surfaces of the structure are in adiabatic condition. The rest of the inner walls are heated isothermally. Computational analysis is carried out for different configurations of the chamber by solving Navier-Stokes and heat energy equations via the finite element approach. Parametric computations are conducted by varying Hartmann numbers ($0 \leq Ha \leq 20$), Rayleigh numbers ($10^3 \leq Ra \leq 10^6$), width of the vertical sections ($0.2 \leq d/L \leq 0.4$, where L denotes the structure's reference dimension), and thickness of the horizontal middle section ($0.2 \leq t/L \leq 0.4$). To find out the impact of the governing parameters on thermal performance for different configurations, the mean Nusselt number along the hot walls, mean temperature of fluid, overall entropy generation, and thermal performance criterion are assessed. In addition, the variations in fluid motion and thermal patterns are reported in terms of streamlines, isotherms, and heatlines. With a larger mean Nusselt number and smaller thermal performance criterion, better heat transmission performance is found for thicker horizontal middle section and wider vertical sections. The maximum reduction in thermal performance criterion is found to be 87.8 % for increasing the width of the vertical sections. However, in the cases of Ha and d/L, there is an interesting transition in Nusselt number noticed for different Rayleigh numbers.

1. Introduction

Since free convection does not require any external energy, it is frequently utilized as a heat transfer mechanism, particularly in straightforward and ordinary systems. Simple examples of free convection heat transmission include ovens, furnaces, building comfort, and even the warm air in a home [1–3]. Several building structures of different shapes undergo thermal mechanisms and cooling to ensure proper building comfort. Similarly, most electrical equipment fitted inside a box is a closed chamber that utilizes free convection for heat dissipation. Numerical simulation is used to analyze and investigate the free convection of such thermal systems. Due to this, numerous studies concentrating on various elements of free convection inside a chamber have drawn the attention of many researchers. The investigation conducted by De Vahl Davis [4] could potentially be considered a groundbreaking study in this field. He used the finite difference method to simulate free convection within a square chamber, where the horizontal walls were maintained in

* Corresponding author.
E-mail address: sumonsaha@me.buet.ac.bd (S. Saha).

https://doi.org/10.1016/j.heliyon.2024.e29380
Received 14 November 2023; Received in revised form 17 February 2024; Accepted 7 April 2024
Available online 10 April 2024

thermal insulation, and the vertical surfaces were differentially heated. The specific outcomes obtained from his study, employing extrapolation techniques, have been integrated into contemporary computer programs as a benchmark problem for modeling free convection. His investigation discovered that the formation of vortices within the chamber intensified with a rise in the Rayleigh number. The findings also demonstrated a direct connection between the mean Nusselt and Rayleigh numbers, revealing increased heat transmission with increasing Rayleigh numbers.

Studying free convection within hollow structures or chambers of various forms is now becoming important in many real-world applications. For this reason, several studies focused on this particular facet. For example, to apply solar collectors, Rahman et al. [5] researched free convective flow in a nanofluid-filled triangular-shaped chamber. Similarly, Chabani et al. [6] studied a hybrid nanofluid's magnetohydrodynamic (MHD) flow in a triangular enclosure with a zigzags inclined wall and an inner elliptic obstacle. On the other hand, Mojumder et al. [7] analyzed ferrofluid's MHD free convective flow within a *C*-shaped chamber. Another similar study focusing on entropy production within a half-moon-shaped chamber was conducted by Mojumder et al. [8]. Recent studies by Tayebi et al. [9,10] showed the natural convective flow of micropolar nanofluid and nano-encapsulated phase change material inside an *I*-shaped domain. Mohebbi et al. [11] later examined free convective flow inside an *Γ*-shaped domain with a rectangle-shaped hot obstacle. The computational model in their study could effectively be utilized to optimize the position of the electronic chip on a printed circuit board (PCB) to facilitate cooling. Raizah et al. [12] investigated the free convection of alumina-water nanofluid in an *E*-shaped domain. This *E*-shaped chamber could be used in isothermal building design and *E*-structured resonator metamaterial for fifth-generation networks. In addition, Saleh et al. [13] researched free convection in an asymmetric *U*-shaped enclosure filled with nano-encapsulated phase change material. Another form of famous geometry, such as an *L*-shaped heat exchanger, was considered by Ferhi et al. [14] under the impact of MHD free convection using the Lattice Boltzmann method. Recently, Jamy et al. [15] also analyzed the conjugate free convective flow within an *L*-shaped chamber filled with water featuring a thick fin subjected to a magnetic field's impact.

The *H*-shaped hollow structure or chamber can be used to ensure internal comfort and cooling of battery-operated or other passive electronic equipment, making it a convenient cooling strategy for different building structures. In addition, the *H*-shaped chamber is ideal for the regulated growth of cells and other biological materials. Due to their versatile applications in various sectors, *H*-shaped hollow structures or chambers have garnered significant attention among researchers. Consequently, numerous research studies were conducted to investigate free convective flow within *H*-shaped chambers. For example, Mansour et al. [16] explored the natural convection of different nanofluids within an *H*-shaped chamber filled with a porous medium. They observed that Cu nanoparticles had the most profound effect on improving heat transmission. Later, Rahimi et al. [17] analyzed the free convective flow of a hybrid nanofluid (SiO_2–TiO_2/water) inside an *H*-shaped chamber using Lattice Boltzmann method. They also studied entropy generation in the system and showed that entropy production was proportional to the Rayleigh number. Keramat et al. [18] analyzed the free convection of nanofluid (alumina-water) within an *H*-shaped chamber with or without having a *V*-shaped baffle. They established that a higher aspect ratio of an *H*-shaped chamber decreased heat transmission. Similar research was conducted by Keramat et al. [19] regarding free convection in an *H*-shaped chamber filled with air and containing porous fins. Loukili et al. [20] studied the free convective flow of air within an *H*-shaped chamber using the Galerkin finite element approach. They demonstrated that higher interior heights resulted in less efficient heat transmission. In a recent study, Raizah and Aly [21] investigated free convective Cu-water nanofluid flow within an *H*-shaped chamber. They noticed that adding nanoparticles decreased the velocity field and improved heat transmission. Table 1 lists all previous studies on free convection within an *H*-shaped chamber.

Research on MHD free convection generates significant utility across various industries and disciplines. When an electrically conductive fluid occupies a chamber, the fluid and heat flow inside the chamber can be regulated by introducing a magnetic field. In the industrial sector, an external magnetic field is used to control crystal development and solidification processes effectively, producing high-quality manufactured goods. Hence, many studies regarding MHD free convection were performed [22–26]. For example, Yuan et al. [22] studied MHD free convective flow and entropy production within a semicircular chamber filled with nanofluid. They found that total entropy production decreased due to increasing Hartmann numbers. Sourtiji and Hosseinizadeh [23] examined MHD free convective flow within an *L*-shaped chamber in an analogous nanofluid investigation. Afterward, Yu et al. [24] studied MHD free convective flow within a rectangular chamber varying the magnitude and direction of the magnetic field. Their simulated findings demonstrated that the angle of inclination influenced heat transport in addition to the intensity of the magnetic field. Recently, Azzawi and Al-damook [25] analyzed MHD free convection within an *M*-shaped chamber. Similarly, Rahmoune and Bougoul [26] examined the MHD natural convective flow of alumina-water nanofluid within a cavity having a wavy wall. According to their findings, the percentage of heat transfer enhanced with the rising Rayleigh number and volume percentage of nanoparticles but diminished with the rising Hartmann number.

Table 1
List of the previously published studies on free convection within an *H*-shaped chamber.

Authors	Fluid(s)	d/L	t/L	Ra
Mansour et al. [16]	Cu-water, Ag-water, Al_2O_3-water, TiO_2-water	$0.2 - 0.5$	$0.2 - 0.8$	$50 - 10^3$
Rahimi et al. [17]	SiO_2–TiO_2-water	0.35	0.4	$10^3 - 10^6$
Keramat et al. [18]	Al_2O_3-water	$0.3 - 0.4$	$0.2 - 0.6$	$10^4 - 10^6$
Keramat et al. [19]	Air	$0.4 - 0.45$	$0.6 - 0.8$	$10^3 - 10^5$
Loukili et al. [20]	Air	0.42	$0.25 - 0.5$	$10 - 10^6$
Raizah and Aly [21]	Cu-water	0.21	0.25	$10^3 - 10^5$

Along with MHD free convection, the effect of Joule heating also attracted several researchers [27–30]. Ghaffarpasand [27] studied the effects of Joule heating on MHD free convective heat transfer within a porous chamber filled with Cu-water nanofluid. Later, Vasu [28] and Gholinia et al. [29] investigated the influences of Joule heating on MHD free convective flow of nanofluid over an inclined surface. Tasnim et al. [30] recently examined a nanofluid's conjugate natural convective flow within a square chamber featuring multiple heat-generating objects. They studied the impact of a magnetic field along with Joule heating.

The examination of entropy generation plays a critical role in enhancing the thermal efficiency of a system through the minimization of irreversibility. Hence, numerous studies have been performed on this issue. For instance, Selimefendigil et al. [31] studied the generation of entropy during MHD free convection within a trapezoid-shaped domain filled with nanofluid. They conducted a second law analysis inside the chamber for several volume fractions of nanoparticles and Hartmann numbers. Li et al. [32] examined entropy generation due to free convection within a square domain under the impact of radiation and magnetic fields. Later, Tayebi et al. [33] studied natural convective flow within a square chamber. The cavity was filled with nanofluid and divided by a solid conductive wall. They investigated the impact of the magnetic field on entropy generation in this study. Similarly, Khetib et al. [34] explored entropy generation on MHD free convection with radiation inside a square chamber filled with MgO–H_2O nanofluid. According to them, not only the heat transfer rate but also the generation of entropy was improved by including radiation as a means of heat transmission. Afterward, Cheng et al. [35] performed a Lattice Boltzmann method-based analysis of the free convection of hybrid nanofluids in a square chamber. They found that a higher inclination of the magnetic field increased the production of frictional entropy, thermal entropy, and overall entropy production. Recently, Mebarek-Oudina et al. [36] researched the free convection of hybrid nanofluid. They investigated the contribution of magnetohydrodynamics and porous media to entropy generation.

The applications of *H*-shaped chambers in thermal and fluid engineering have garnered significant attention in the existing literature, as evidenced by numerous studies [16–21]. Despite the extensive research on *H*-shaped chambers, a critical gap exists in exploring entropy production resulting from MHD free convection within such chambers, particularly when considering the variable dimensions and the impact of Joule heating. The absence of prior investigations in this domain highlights the need for a comprehensive understanding of the thermodynamic implications associated with the interplay of magnetic fields, free convection, and geometric variations within an *H*-shaped hollow structure. Various technological applications crucially depend on the principles of free convection within *H*-shaped chambers, including but not limited to thermal energy storage, bioreactors, solar thermal collectors, and microfluidic devices. Therefore, this study aims to contribute to the existing knowledge by examining the intricate effects of Joule heating and geometric variations on entropy generation and thermal performance within the *H*-shaped chamber. Through a rigorous numerical analysis encompassing diverse governing and geometric parameters, qualitative and quantitative outcomes will be presented to elucidate the multifaceted influences of these parameters on the system's behavior.

Furthermore, the current research proposes optimal dimensions and Hartmann numbers to ensure enhanced thermal performance with minimal energy input. This study chooses the optimum parameters based on the thermal performance criterion instead of the mean Nusselt number. It accounts for the contribution of total entropy generation per unit change of the mean Nusselt number. Thus, it is helpful to identify maximum heat transfer performance and minimum energy input. By identifying and optimizing these key parameters, the study aims to provide valuable insights for designing *H*-shaped chambers that exhibit superior thermal efficiency, thereby contributing to fluid mechanics and thermal engineering advancements. The outcomes of this investigation are anticipated to inform the development of more efficient and sustainable systems across a range of applications, aligning with the broader goals of improving energy utilization and promoting environmentally conscious engineering practices.

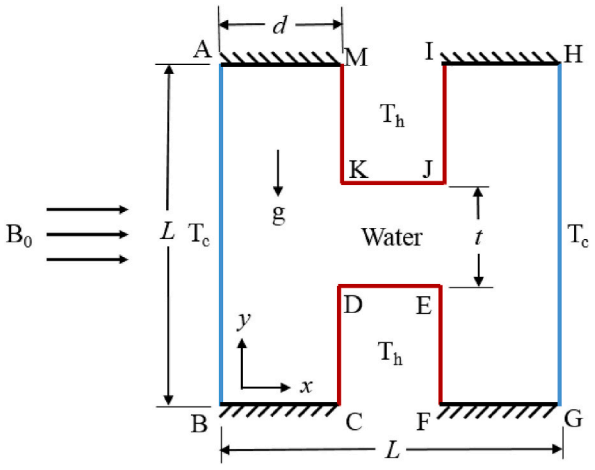

Fig. 1. Two-dimensional schematic diagram of the *H*-shaped chamber (color online). (For interpretation of the references to color in this figure legend, the reader is referred to the Web version of this article.)

2. Model description

The physical model ABCDEFGHIJKM utilized for the current problem depicting an *H*-shaped chamber with its dimensions and boundary conditions is displayed in Fig. 1. In a Cartesian framework, the two-dimensional *H*-shaped chamber has an origin at point B, and its length is equal to AB = BG = $L = 0.05$ m. The left surface AB and the right surface GH of the chamber are kept at the invariant surrounding temperature T_c, while CDEF and IJKM are kept at a relatively higher temperature T_h ($>T_c$). The remaining walls are thermally insulated, and their lengths are equivalent to BC = FG = IH = AM = d. The height of the middle section is equal to t, as shown in Fig. 1 [18]. The chamber is occupied by water having the following properties: mass density $\rho = 997$ kg/m^3, constant pressure specific heat $C_p = 4180$ J/kg.K, dynamic viscosity $\mu = 8.91 \times 10^{-4}$ Pa.s, volumetric thermal expansion coefficient $\beta = 2.47 \times 10^{-4}$ 1/K and thermal conductivity $k = 0.607$ W/m.K at mean temperature of $T_m = 25$ °C [37]. The chamber is affected by a horizontally applied magnetic field B_0 on the left vertical wall, whereas the gravitational field (g) acts downward.

This study considers the two-dimensional mass continuity, momentum conservation, and heat energy equations incorporating Joule heating and MHD impact. Other factors like radiation, internally generated heat, and any dissipation from fluid viscosity are considered insignificant. With these assumptions in mind, the mathematical equations of the existing problem can be expressed as follows [30]:

$$\frac{\partial u}{\partial x}+\frac{\partial v}{\partial y}=0, \tag{1}$$

$$\rho\left(u\frac{\partial u}{\partial x}+v\frac{\partial u}{\partial y}\right)=-\frac{\partial p}{\partial x}+\mu\left(\frac{\partial^2 u}{\partial x^2}+\frac{\partial^2 u}{\partial y^2}\right), \tag{2}$$

$$\rho\left(u\frac{\partial v}{\partial x}+v\frac{\partial v}{\partial y}\right)=-\frac{\partial p}{\partial y}+\mu\left(\frac{\partial^2 v}{\partial x^2}+\frac{\partial^2 v}{\partial y^2}\right)+\rho g\beta(T-T_c)-\sigma B_0^2 v, \tag{3}$$

$$\rho C_p\left(u\frac{\partial T}{\partial x}+v\frac{\partial T}{\partial y}\right)=k\left(\frac{\partial^2 T}{\partial x^2}+\frac{\partial^2 T}{\partial y^2}\right)+\sigma B_0^2 v^2. \tag{4}$$

In these governing equations, (x, y) represents the Cartesian coordinates, while (u, v) corresponds to the components of velocity in the respective coordinates. Other variables, for example, T and p, also stand for temperature and pressure, respectively, and σ is the electrical conductivity of water. The non-dimensional representation of the above equations (1)–(4) can be given below:

$$\frac{\partial U}{\partial X}+\frac{\partial V}{\partial Y}=0, \tag{5}$$

$$U\frac{\partial U}{\partial X}+V\frac{\partial U}{\partial Y}=-\frac{\partial P}{\partial X}+Pr\left(\frac{\partial^2 U}{\partial X^2}+\frac{\partial^2 U}{\partial Y^2}\right), \tag{6}$$

$$U\frac{\partial V}{\partial X}+V\frac{\partial V}{\partial Y}=-\frac{\partial P}{\partial Y}+Pr\left(\frac{\partial^2 V}{\partial X^2}+\frac{\partial^2 V}{\partial Y^2}\right)+RaPr\Theta-Ha^2PrV, \tag{7}$$

$$U\frac{\partial \Theta}{\partial X}+V\frac{\partial \Theta}{\partial Y}=\frac{\partial^2 \Theta}{\partial X^2}+\frac{\partial^2 \Theta}{\partial Y^2}+JV^2. \tag{8}$$

Here, X, Y, U, V, P, and Θ are the respective dimensionless variables of x, y, u, v, p, and T. The following scales (9) are utilized to perform the above dimensional analysis and obtain the dimensionless mathematical model (5)–(8):

Table 2
Auxiliary conditions of the current problem.

Boundary	Dimensional Condition		Dimensionless Condition	
	Velocity	Temperature	Velocity	Temperature
AB	$u = v = 0$	$T = T_c$	$U = V = 0$	$\Theta = 0$
BC	$u = v = 0$	$\partial T/\partial y = 0$	$U = V = 0$	$\partial\Theta/\partial Y = 0$
CD	$u = v = 0$	$T = T_h$	$U = V = 0$	$\Theta = 1$
DE	$u = v = 0$	$T = T_h$	$U = V = 0$	$\Theta = 1$
EF	$u = v = 0$	$T = T_h$	$U = V = 0$	$\Theta = 1$
FG	$u = v = 0$	$\partial T/\partial y = 0$	$U = V = 0$	$\partial\Theta/\partial Y = 0$
GH	$u = v = 0$	$T = T_c$	$U = V = 0$	$\Theta = 0$
HI	$u = v = 0$	$\partial T/\partial y = 0$	$U = V = 0$	$\partial\Theta/\partial Y = 0$
IJ	$u = v = 0$	$T = T_h$	$U = V = 0$	$\Theta = 1$
JK	$u = v = 0$	$T = T_h$	$U = V = 0$	$\Theta = 1$
KM	$u = v = 0$	$T = T_h$	$U = V = 0$	$\Theta = 1$
MA	$u = v = 0$	$\partial T/\partial y = 0$	$U = V = 0$	$\partial\Theta/\partial Y = 0$

$$[X,Y]=\frac{[x,y]}{L},[U,V]=\frac{[u,v]L}{\alpha},P=\frac{pL^2}{\rho\alpha^2},\Theta=\frac{T-T_c}{T_h-T_c}, \tag{9}$$

where α is thermal diffusivity of water. Besides, the dimensionless governing parameters like Prandtl number, Rayleigh number, Hartmann number, and Joule heating parameter are respectively defined as follows (10):

$$Pr=\frac{C_p\mu}{k},Ra=\frac{g\beta\rho^2(T_h-T_c)L^3}{\mu^2}Pr,Ha=B_0L\sqrt{\frac{\sigma}{\mu}},J=\frac{g\beta LHa^2}{C_pRa}. \tag{10}$$

The dimensional and dimensionless auxiliary conditions of the current problem are listed in Table 2.

To find out the system's performance under MHD free convection, the individual mean Nusselt number (Nu_s) along a heated surface can be calculated as [30]:

$$Nu_s=-\frac{L}{L_e(T_h-T_c)}\int_0^{L_e}\frac{\partial T}{\partial n}ds=-\frac{L}{L_e}\int_0^{L_e/L}\frac{\partial\Theta}{\partial N}dS, \tag{11}$$

where L_e is the length of the corresponding heated surface, s and S denote dimensional and dimensionless surface lengths, respectively, and n and N are the wall-normal distances in dimensional and dimensionless forms, respectively. The mean Nusselt number (Nu) for this problem can be evaluated by averaging the individual mean Nusselt number (11) along six hot walls (CD, DE, EF, IJ, JK, and KM) as follows [30]:

$$Nu=\frac{\sum Nu_s}{6}. \tag{12}$$

Furthermore, to assess the heat transfer performance of the chamber, it is essential to determine the mean fluid temperature within the whole domain. Therefore, the non-dimensional mean fluid temperature (Θ_{av}) is computed through the following equation (13):

$$\Theta_{av}=\frac{L^2}{a}\int_A\left(\frac{T-T_c}{T_h-T_c}\right)dxdy=\frac{L^2}{a}\int_A\Theta dXdY, \tag{13}$$

where a is the surface area of the computational domain. Entropy production demonstrates the importance of irreversible factors in processes such as heat transfer, fluid friction, and various other deviations from an ideal system behavior. It quantifies the energy transmission and evaluates the thermal efficiency representing the loss of energy. In free convective flow involving the magnetohydrodynamic effect, entropy generation occurs due to viscous dissipation, heat transfer, and the impact of the applied magnetic field. The local entropy generation caused by heat transfer (s_{ht}) can be determined using the following relationship [30]:

$$s_{ht}=\frac{k}{T^2}\left[\left(\frac{\partial T}{\partial x}\right)^2+\left(\frac{\partial T}{\partial y}\right)^2\right]. \tag{14}$$

Additionally, the entropy generation owing to the friction of fluid is influenced by the velocity gradient, particularly near the wall where the interaction between the vortices rotating in convective flow is expected to be more prominent. The local entropy generation owing to the dissipation of fluid flow (s_{ff}) and the presence of a magnetic field (s_{mf}) can be represented as follows [30]:

$$s_{ff}=\frac{\mu}{T}\left[2\left(\frac{\partial u}{\partial x}\right)^2+2\left(\frac{\partial v}{\partial y}\right)^2+\left(\frac{\partial u}{\partial y}+\frac{\partial v}{\partial x}\right)^2\right], \tag{15}$$

$$s_{mf}=B_0^2\frac{\sigma}{T}v^2. \tag{16}$$

To get the dimensionless local entropy production, the following reference entropy is used:

$$s_{ref}=k\left(\frac{T_h-T_c}{T_cL}\right)^2. \tag{17}$$

Using (17), the non-dimensional forms of local entropy production (S_{ht}, S_{ff}, and S_{mf}) can be obtained from (14)-(16) as follows:

$$S_{ht}=\left(\frac{T_c}{T}\right)^2\left[\left(\frac{\partial\Theta}{\partial X}\right)^2+\left(\frac{\partial\Theta}{\partial Y}\right)^2\right]. \tag{18}$$

$$S_{ff}=\varphi\left[2\left(\frac{\partial U}{\partial X}\right)^2+2\left(\frac{\partial V}{\partial Y}\right)^2+\left(\frac{\partial U}{\partial Y}+\frac{\partial V}{\partial X}\right)^2\right],\varphi=\frac{\mu}{kT}\left[\frac{\alpha T_c}{L(T_h-T_c)}\right]^2, \tag{19}$$

$$S_{mf}=\varphi Ha^2V^2, \tag{20}$$

where φ is the irreversibility coefficient obtained from the thermo-physical properties of water, boundary wall temperatures, fluid temperature, and the reference length of the physical model. The dimensionless overall entropy generation (S_T) is evaluated from (18)-(20) using the following equation [30,38]:

$$S_T = \frac{L^2}{a}\int_A \left(S_{ht} + S_{ff} + S_{mf}\right) dXdY. \tag{21}$$

The evaluation of the total generation of entropy relative to heat transfer can be achieved by employing the thermal performance criterion (*TPC*) as shown below [30,38]:

$$TPC = \frac{S_T}{Nu}. \tag{22}$$

To visualize the paths of fluid flow and heat transfer within the enclosure, streamline and heatline have been provided during the qualitative analysis. They depend on the stream function and the heat function inside the cavity. The equations for stream function (Ψ) and heat function (H) in non-dimensional forms are outlined below [17]:

$$\nabla^2\Psi = \frac{\partial U}{\partial Y} - \frac{\partial V}{\partial X}, \tag{23}$$

$$\nabla^2 H = \frac{\partial (U\Theta)}{\partial Y} - \frac{\partial (V\Theta)}{\partial X}. \tag{24}$$

3. Numerical procedure and verification

The finite element method is employed to solve equations (1)–(4) and the required auxiliary conditions for the current problem. For numerical solutions, COMSOL Multiphysics 6.1, a commercial CFD package that simulates based on the Galerkin finite element approach, is utilized in this study. This software is well-known for its accuracy and consistency, as it has been used extensively in several previous studies [39–43]. The entire domain of interest is discretized using triangular meshes with different sizes of elements. A grid-independent test is conducted to ensure the computational analysis's precision, as demonstrated in Fig. 2. It is visible that the mean Nusselt number obtained from (12) gets less responsive to further refinement after reaching an optimum number of elements (N_E). The mean Nusselt number computed at $Ra = 10^6$, $Ha = 20$, $d/L = 0.4$, and $t/L = 0.4$ becomes nearly invariant for $N_E \geq 26596$ (see Fig. 2). Hence, the optimum element number utilized for this case of computational simulation is determined as $N_E = 26596$, referred to as the "**Extra Fine Mesh**" in the software being used. When the dimensions of the geometry vary, the optimum number of elements also varies. Hence, by conducting a similar grid independence test, the optimal number of mesh elements is determined for other geometric arrangements of the problem, as presented in Table 3.

Verifying the outcome of the mathematical model and simulation tool against the previous literature before utilizing it in any computational analysis is essential to ensure accuracy and reliability. In this regard, the results of the current model and simulation software are compared to the numerical analyses conducted by Keramat et al. [18] and Sourtiji and Hosseinizadeh [23]. The variation in the mean Nusselt number between the present model and the previous literature is depicted in Fig. 3, with the Rayleigh number as the governing parameter. For further assurance, the current model is validated by correlating the results between the present simulation and the experimental study performed by Corvaro and Paroncini [44]. The outcomes are presented in terms of the velocity map and streamline plots, as shown in Fig. 4. The results obtained from the present model exhibit a reasonable agreement with those obtained in both numerical (Fig. 3) and experimental (Fig. 4) studies performed previously and thus providing a level of confidence for conducting further simulations with a similar configuration. This comparison affirms the computational tool's accuracy and validity

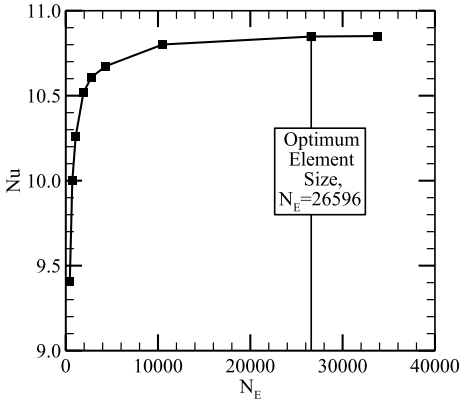

Fig. 2. Grid independent test at $d/L = 0.4$, $t/L = 0.4$, $Ra = 10^6$ and $Ha = 20$.

Table 3
Optimum mesh size for an *H*-shaped chamber with different dimensions.

d/L	t/L	N_E
0.2	0.2	24062
0.2	0.3	24360
0.2	0.4	24148
0.3	0.2	25966
0.3	0.3	26050
0.3	0.4	25742
0.4	0.2	27370
0.4	0.3	26926
0.4	0.4	26596

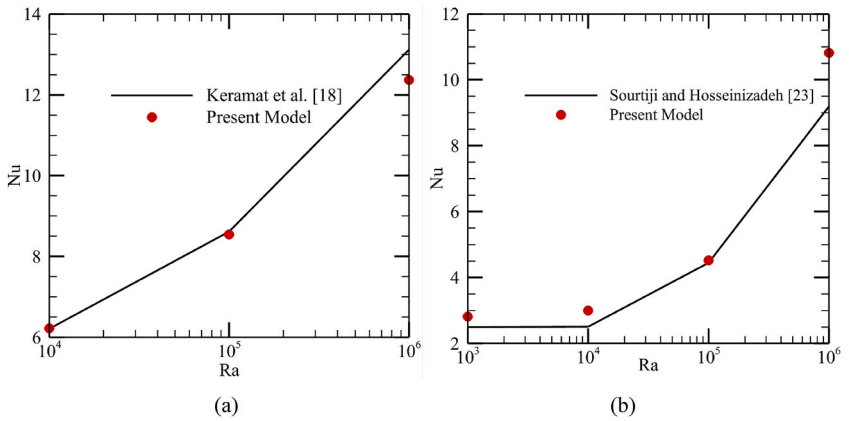

Fig. 3. Validation of the current model by comparing with the outcomes of (a) Keramat et al. [18] and (b) Sourtiji and Hosseinizadeh [23] via the distribution of mean Nusselt number (color online). (For interpretation of the references to color in this figure legend, the reader is referred to the Web version of this article.)

and verifies the mathematical model's correct utilization.

4. Results and discussions

The present study focuses on investigating the effects of Joule heating and magnetic field on natural convection in an *H*-shaped chamber. Parametric simulations are considered for an extensive spectrum of Hartmann numbers ($0 \leq Ha \leq 20$), Rayleigh numbers ($10^3 \leq Ra \leq 10^6$), the dimensionless width of the vertical sections ($0.2 \leq d/L \leq 0.4$), and the dimensionless length of the horizontal middle section ($0.2 \leq t/L \leq 0.4$) of the chamber. Performance parameters such as the mean Nusselt number, overall entropy generation, thermal performance criterion, and mean temperature of the fluid are calculated to assess the impact of the geometric and governing parameters on the heat transfer performance of the system. Initially, the Hartmann number is varied while keeping the dimensions fixed aiming to determine the optimal Hartmann number for achieving the maximum performance of heat transfer. Subsequently, the optimum Hartmann number is held constant while modifying the chamber's dimensions to identify the optimal chamber configuration. This approach allows one to follow a one-point optimization process for the precise evaluation of the impacts of different geometric and governing parameters on the system's thermal characteristics. Finally, the visualization of fluid and heat flow patterns inside the chamber is depicted through isotherm, streamline, and heatline plots for the optimum condition and configuration.

4.1. *Effect of changing strength of magnetic field*

Fig. 5 represents the alteration of the mean Nusselt number, mean fluid temperature, overall entropy generation, and *TPC* for changing Rayleigh and Hartmann numbers, where both d/L and t/L are constant at 0.4. Fig. 5(a) demonstrates the distribution in the mean Nusselt number with the increasing *Ra* and *Ha*. In this case, the mean Nusselt number exceeds unity, indicating the dominance of convection heat transfer. For any scenario (any value of *Ha*), the mean Nusselt number stays relatively constant when the Rayleigh number is small ($Ra \leq 10^4$). However, it increases significantly with the rise in Rayleigh number regardless of the Hartmann number value. When the Hartmann number rises, there is a noticeable drop in the mean Nusselt number, particularly at larger Rayleigh numbers. This occurs because the induced magnetic field consistently hinders the fluid motion within the chamber, which intensifies with higher Hartmann numbers. The maximum deviation of the mean Nusselt number with the change of Hartmann number from $Ha = 0$ to $Ha = 20$ is 21.5 % at $Ra = 5 \times 10^4$.

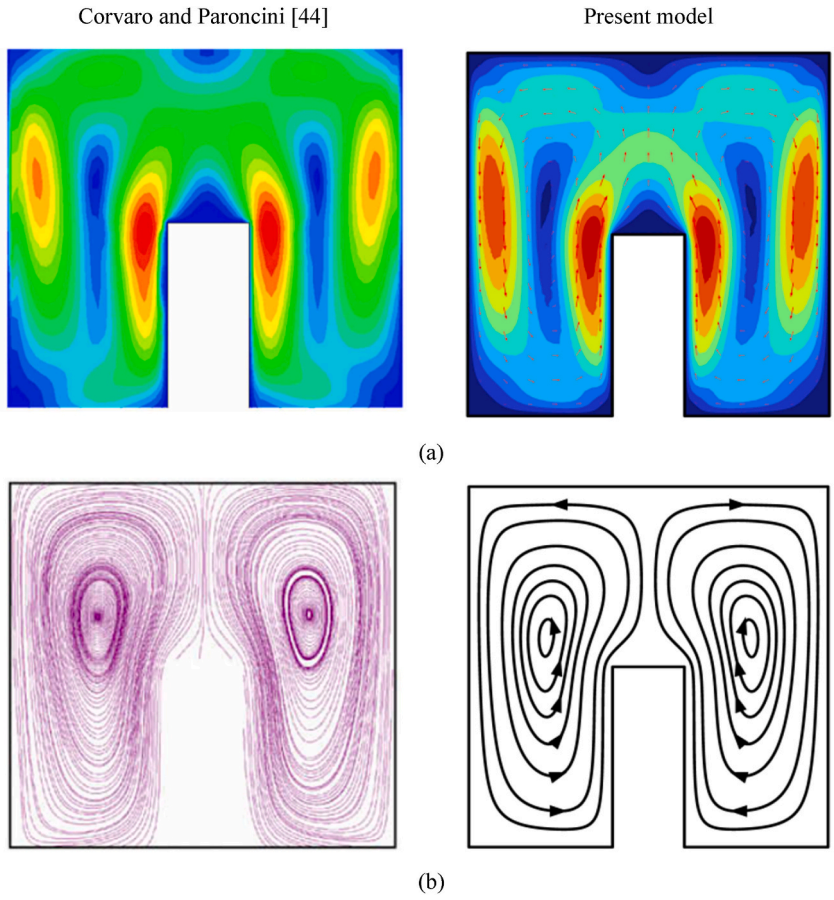

Fig. 4. Verification of the present model using the experimental results of Corvaro and Paroncini [44] employing (a) velocity map and (b) streamlines at $Ra = 6.39 \times 10^4$ and Pr = 0.7296 (color online). (For interpretation of the references to color in this figure legend, the reader is referred to the Web version of this article.)

The relationship among average fluid temperature, Rayleigh number, and Hartmann number is depicted in Fig. 5(b). At higher Rayleigh numbers, the average fluid temperature decreases. This occurs because of the increased dominance of convective heat transfer, which efficiently redistributes heat and reduces temperature gradients within the fluid. This also conforms the result found in Fig. 5(a) indicating better thermal performance at higher Rayleigh numbers. The impact of the Hartmann number on mean fluid temperature is less significant at lower *Ra* when the buoyancy force is relatively low. In this regime, the impact of the magnetic field (specified by *Ha*) on average fluid temperature is relatively minor because the convective motion is not strong enough to show significant temperature variation. However, Θ_{av} starts to suppress the convective motion with the increasing *Ha* and thus conforming to the findings of Fig. 5(a).

Fig. 5(c) displays the relationship of total entropy generation (calculated using (21)) with changing Rayleigh and Hartmann numbers. The profiles of total entropy generation are similar to those of the overall Nusselt number. At smaller Rayleigh numbers, the entropy generation is essentially invariant and minimum. However, with an augmentation in Rayleigh number, heat transfer due to convection becomes enhanced, leading to a significant rise in entropy production. Higher Rayleigh numbers indicate stronger buoyancy-driven flow, promoting vigorous fluid motion and more efficient heat transfer, reducing temperature gradients and increasing entropy generation. On the contrary, a rise in the Hartmann number suppresses fluid motion due to the induced magnetic field, resulting in reduced mixing and diffusion of heat, eventually decreasing entropy generation. The reduction in fluid velocity and mixing speed at higher Hartmann numbers also decreases irreversibility, further contributing to the decrease in entropy generation.

Fig. 5(d) shows the alteration in *TPC* evaluated from (22) with the change of *Ra* and *Ha*. The profiles of *TPC* in this curve show an exciting trend, indicating two different regions of operation for selecting the optimum Hartmann number. It is visible that at lower *Ra* ($\leq 3 \times 10^3$), the Hartmann number less dominantly affects the *TPC*. This happens because the buoyancy force is low at lower Rayleigh numbers, and any change in the Hartmann number only alters the conduction process. However, at greater Rayleigh numbers, the impact of the Hartmann number becomes significant. Due to the larger buoyancy force and strong fluid circulation, varying the Hartmann number pointedly affects the fluid motion, and there is a noticeable variation in *TPC,* as presented in Fig. 5(d). Moreover, it can be noticed from Fig. 5(d) that the lower Hartmann number ($Ha = 0$) ensures minimum *TPC* at higher Rayleigh numbers ($Ra > 3 \times 10^3$) due to the contribution of *Nu* with *Ra* and *Ha*, whereas at the conduction regime, the highest value of *Ha* (=20) ensures the lowest

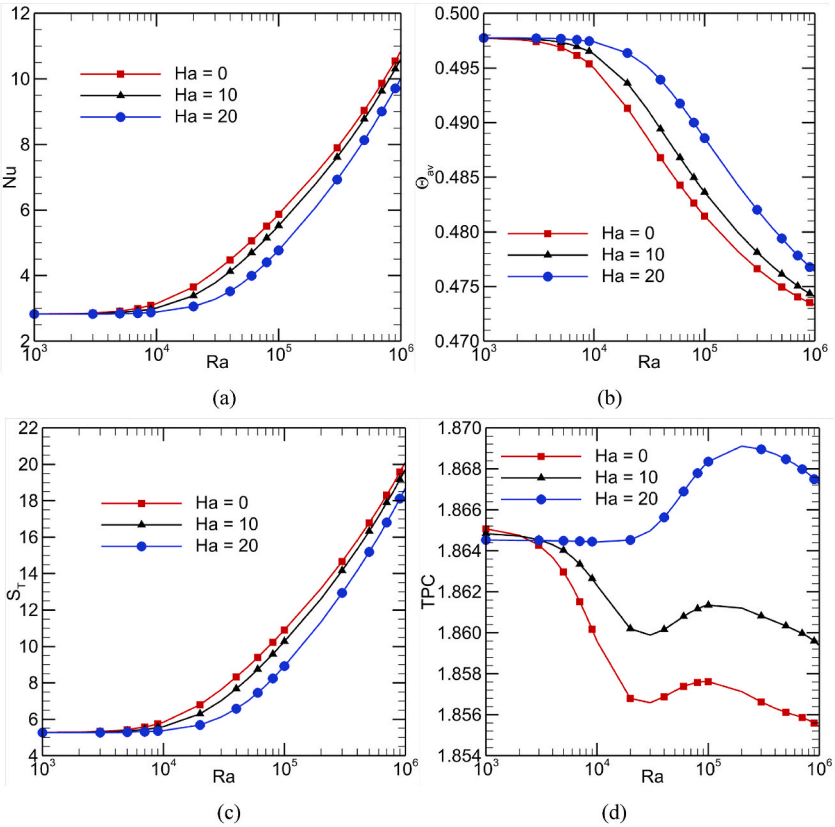

Fig. 5. The variation in (a) *Nu*, (b) Θ_{av}, (c) S_T, and (d) *TPC* for various *Ha* with *Ra* at $d/L = 0.4$ and $t/L = 0.4$ (color online). (For interpretation of the references to color in this figure legend, the reader is referred to the Web version of this article.)

TPC. However, the deviation of *TPC* values between $Ha = 0$ and 20 is only 0.67 % at most, reflecting less alteration compared to the mean Nusselt number.

4.2. *Effect of changing width of vertical section of chamber*

Fig. 6 indicates the variation in the mean Nusselt number, mean fluid temperature, overall entropy generation, and *TPC* for different d/L ratios and *Ra* while maintaining the Hartmann number constant at 0 and 20, respectively, and $t/L = 0.4$. In Fig. 6(a), the mean Nusselt number shows an interesting pattern. A lower d/L ratio leads to a larger mean Nusselt number at lower Rayleigh numbers. However, this relationship reverses beyond a Rayleigh number of 4×10^4, and a higher d/L ratio is associated with a higher mean Nusselt number. This shift occurs due to the combined influence of the enhancement of free convection and the reduction of heat source length. At lower Rayleigh numbers, a narrower section promotes more substantial conductive heat transfer due to close contact between the source and the sink, although the size of the heat source becomes larger. In contrast, at higher Rayleigh numbers, a wider section (high d/L) counteracts the suppressive effect of increasing distance between the source and the sink by the higher heat sink length, resulting in a massive convective cooling effect. A maximum 33.7 % improvement of the mean Nusselt number is observed for a change of d/L from 0.4 to 0.2 at $Ra = 10^3$.

In Fig. 6(b), it is apparent that the mean fluid temperature exhibits significant variations with the change in the d/L ratio corresponding to different Rayleigh numbers. Specifically, a lower d/L ratio is associated with a higher average fluid temperature, while a rise in the d/L ratio leads to a drop in the average water temperature. This behavior can be explained by the dominance of free convection in the convective heat transfer process and the involvement of a larger volume of fluid. A lower d/L ratio, representing a narrower vertical part of the chamber, facilitates a high-speed fluid flow and enhances heat transfer. The intensified fluid motion carries more heat away from the hot regions, resulting in a higher average water temperature. Conversely, as the d/L ratio increases, the wider horizontal section allows for a larger spread of water, leading to reduced fluid velocity. Additionally, this configuration results in a smaller area of the hot surface, contributing to the decrease in the average water temperature.

Similarly, in Fig. 6(c)–a noticeable shift in entropy generation is observed after reaching a Rayleigh number of 10^4. The observed shift in entropy generation with changing Rayleigh numbers and d/L ratios can be explained by the interplay between dominant free convection and the change of heat source length. At low Rayleigh numbers, heat conduction becomes the dominant mode of heat transfer inside the chamber. In this case, the entropy generation is lower when the d/L ratio is higher. At higher d/L, the temperature

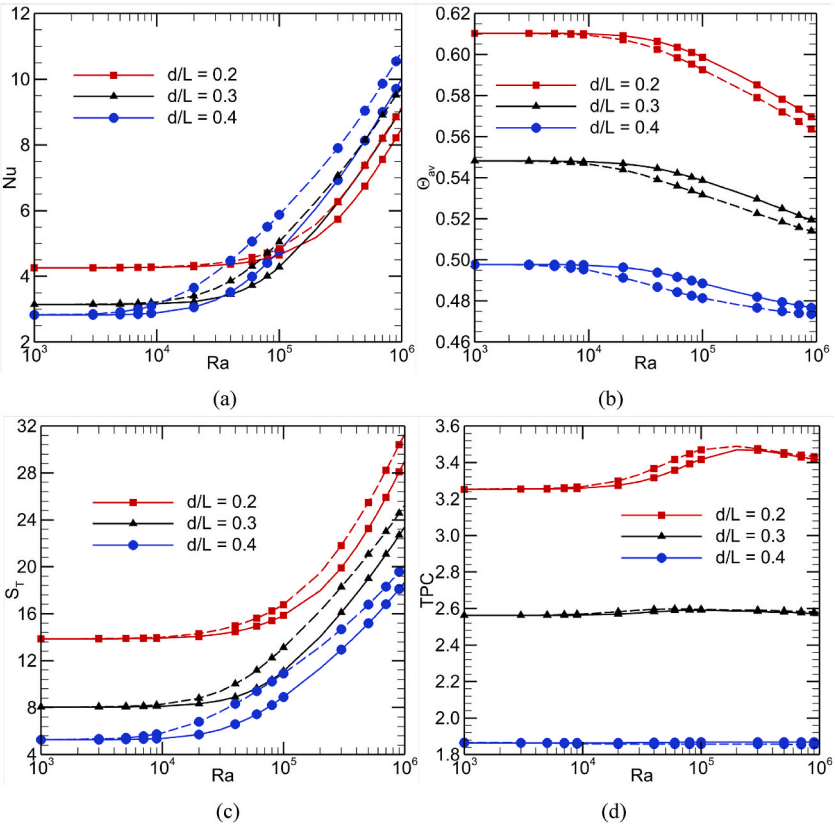

Fig. 6. The variation in (a) *Nu*, (b) Θ_{av}, (c) S_T, and (d) *TPC* with *Ra* for different *d/L* at *t/L* = 0.4. The solid lines indicate the data for *Ha* = 20, whereas the dashed lines are the same for *Ha* = 0 (color online). (For interpretation of the references to color in this figure legend, the reader is referred to the Web version of this article.)

gradient across the chamber becomes more significant, leading to lower heat conduction and, consequently, lower entropy generation. At high Rayleigh numbers, natural convection plays a dominant role in heat transfer. When the *d/L* ratio is low, the distance between the hot and cold walls becomes smaller than the chamber length. However, the size of the heat source rises proportionally and causes a reduction of convective heat transfer at a larger Rayleigh number. As a result, with low *d/L* ratios, there is a higher entropy generation at higher Rayleigh numbers.

Fig. 6(d) represents the shifting behavior for *TPC* with varying *Ra* and *d/L* ratios. As the *Ra* augments, there is a transition from dominant heat conduction to natural convection. It leads to the change in entropy generation and *Nu,* as shown in Fig. 6(a) and (c). In this scenario, the change in entropy generation dominates the behavior of *TPC*. Because, with the rise in *Ra*, the order of the change in *Nu* is lower than that of the change in S_T. Besides, with the increase in *Ra*, the impact of entropy generation is quite significant for *d/L* = 0.2. Finally, it can be concluded that minimum *TPC* is attainable for the case of *d/L* = 0.4, irrespective of the variation of both *Ra* and *Ha*. The highest deviation of *TPC* between *d/L* = 0.2 and *d/L* = 0.4 is 87.8 % at $Ra = 2 \times 10^5$.

4.3. *Effect of changing height of middle section of chamber*

The alteration in the mean Nusselt number, mean fluid temperature, overall entropy generation, and *TPC* for different magnitudes of *t/L* ratio as a function of *Ra* is presented in Fig. 7. All variations are shown at *Ha* = 0 and 20, and *d/L* = 0.4. In Fig. 7(a), the mean Nusselt number rises with a rise in *Ra* and *t/L* ratio. When the *t/L* ratio increases, representing the height of the middle section relative to the chamber's overall size, it reduces the area of the hot surface. Consequently, there is a larger cold surface area than the heated surface for effective convection and additional fluid flow pathways. This enhances convective heat transfer, leading to a higher Nusselt number. A maximum rise of 23.2 % in the mean Nusselt number is observed when *t/L* varies from 0.2 to 0.4.

Fig. 7(b) depicts the impacts of changing *Ra* and *t/L* ratios on the mean fluid temperature. In this case, the mean fluid temperature decreases with the increasing *t/L* ratio. Increasing the *t/L* ratio provides more space for fluid flow, promoting better mixing and convective heat transfer. It results in a decreased average water temperature, which confirms the findings of Fig. 7(a).

Fig. 7(c) illustrates the total entropy generation for varying Rayleigh numbers and *t/L* ratios. For lower Rayleigh numbers, the fluid speed is not significantly affected by the *t/L* ratio, and the variation of entropy generation remains relatively less with changing the *t/L* ratios. With increased *Ra*, entropy generation is higher at lower *t/L* ratios. Because, in lower *t/L* ratios, the middle section of the cavity

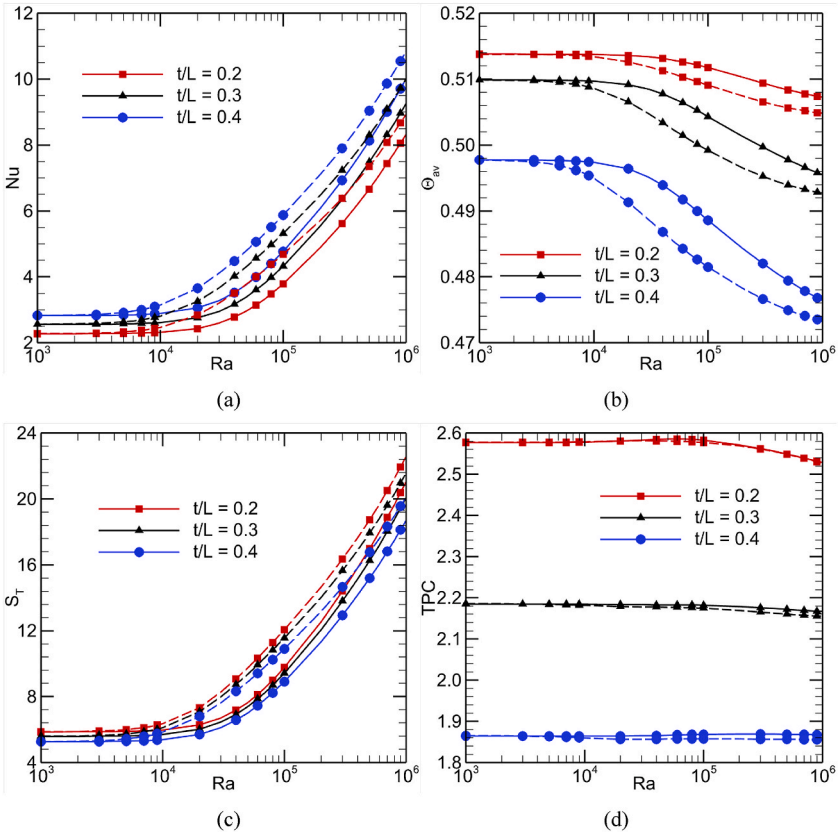

Fig. 7. The variation in (a) *Nu*, (b) Θ_{av}, (c) S_T, and (d) *TPC* with *Ra* for different *t/L* at *d/L* = 0.4. The solid lines indicate the data for *Ha* = 20, whereas the dashed lines are the same for *Ha* = 0 (color online). (For interpretation of the references to color in this figure legend, the reader is referred to the Web version of this article.)

is narrower, and the fluid is confined within a smaller space. As the fluid moves from the hot to the cold walls and vice versa, it experiences more interactions and mixing due to the constrained geometry. This increased mixing results in higher velocity gradients and vortices within the fluid and increases entropy generation. Conversely, a larger *t/L* ratio provides a wider middle section, allowing more convective flow since the area of the heated surface reduces, resulting in a larger area of the cold surface compared to the area of the hot surface. It helps to distribute the temperature more uniformly, reducing temperature gradients and lowering entropy generation.

Fig. 7(d) represents the changes in *TPC* for different *Ra* and *t/L* ratios. It is observed that *TPC* decreases significantly with increasing *t/L* ratios. A higher *t/L* ratio corresponds to a wider middle section in the *H*-shaped chamber, and the ratio of the surface area of the heat sink and that of the heat source becomes higher. Besides, when the *t/L* ratio increases, the vertical space for fluid flow increases, and more area is used to cool down the heated surface. Therefore, it improves convective heat transfer by allowing better mixing and reduction of temperature gradients. Consequently, the mean Nusselt number gets higher, and the entropy production decreases, resulting in a lower *TPC*. It is found that the change of the *t/L* ratio from 0.2 to 0.4 results in the highest deviation of *TPC* at about 39 %.

4.4. Summary of optimized condition

An overall assessment of the existing problem is illustrated in Table 4, showing the maximum thermal performance (minimum *TPC*) for different cases considered in the current investigation. In the case of *Ha*, when *Ra* is less than 3×10^3, thermal performance increases with increasing *Ha*. However, if $Ra > 3 \times 10^3$, thermal performance decreases with increasing *Ha*. Besides, the change in

Table 4
Optimum conditions observed for different Rayleigh numbers in the current problem.

Parameters	$Ra \leq 3 \times 10^3$	$Ra > 3 \times 10^3$
Ha	20	0
d/L	0.4	0.4
t/L	0.4	0.4

thermal performance at a higher Rayleigh number is not very significant with the variation of the Hartmann number. Within the range of *Ra*, *TPC* reduces by a maximum of 0.67 % for altering Hartmann numbers from 0 to 20. In the case of changing *d/L* ratios, thermal performance increases with a larger *d/L* ratio throughout the variation of *Ra*. The variation of *TPC* for varying *d/L* is a maximum of 87.8 % at $Ra = 2 \times 10^5$. Similarly, thermal performance increases with the increasing *t/L* ratio for any value of *Ra*.

4.5. Visualization of qualitative outcomes

To graphically illustrate the changes in thermo-fluid phenomena, various Hartmann ($Ha = 0$ and 20) and Rayleigh ($Ra = 10^4$, 10^5, and 10^6) numbers have been chosen, where *d/L* and *t/L* are kept constant at 0.4 as these are the optimum dimensions according to the quantitative analysis. The contour illustrations for the stream function, temperature, and heat function depicted in Figs. 8–10 visually present the qualitative demonstration of the thermal and flow fields under the optimized conditions and configuration.

Fig. 8 illustrates the streamline patterns (contour plots of stream function calculated using (23)) corresponding to the variation of *Ra* and *Ha*. The results demonstrate the formation of two distinct vortex regions within the chamber. The left vortex exhibits a counter-clockwise rotation, while the right vortex rotates clockwise, primarily influenced by the buoyancy force generated by the thermal gradient. When the Rayleigh number rises, the convective core expands due to enhanced buoyancy effects. Moreover, the interaction among these counter-rotating convective cells gets more pronounced at higher Rayleigh numbers. Conversely, when the Hartmann number is elevated, the magnetic field becomes significant and exerts Lorentz force that impedes the flow motion, resulting in reduced convective effects. Consequently, the flow becomes more streamlined and stable due to the impact of the magnetic field, leading to a drop in the mixing mechanism. The interplay between these effects dictates the prevailing flow characteristics in situations where both the magnetic field and buoyancy forces are prominent. The strong magnetic field modifies the convective patterns, suppressing fluid motion and yielding more organized and directed flow streams. At lower Rayleigh numbers, Hartmann numbers have no significant effect on the flow field. However, at higher Rayleigh numbers, streamline is less intense at the core region for higher Hartmann numbers due to the resistance of magnetic force over buoyancy-driven free convective force. As a result, the heat transfer rate alters accordingly, as shown in Fig. 5(a).

Fig. 9 shows the changes in the iso-surface thermal field via the contour surface plots of temperature with varying Rayleigh and Hartmann numbers. When both Hartmann and Rayleigh numbers are low, the thermal field reflects conduction-dominated patterns with vertical parallel contour lines. Increasing the Rayleigh number while keeping the Hartmann number constant enhances buoyancy, leading to the formation of thermal plumes and intricate contours. Conversely, with a high Hartmann number and a low Rayleigh number, the thermal field becomes more streamlined and stable due to the magnetic field's suppression of fluid motion. When both Rayleigh and Hartmann numbers are high, the thermal field exhibits complex distributions, with the magnetic field organizing the flow into directed streams with well-defined contours. At larger Rayleigh numbers, a distinct difference is observed for the effect of Hartmann numbers, as indicated in Fig. 9(b) and (c).

Fig. 10 illustrates the heatline patterns (contour plots of heat function evaluated from (24)) within the *H*-shaped chamber for

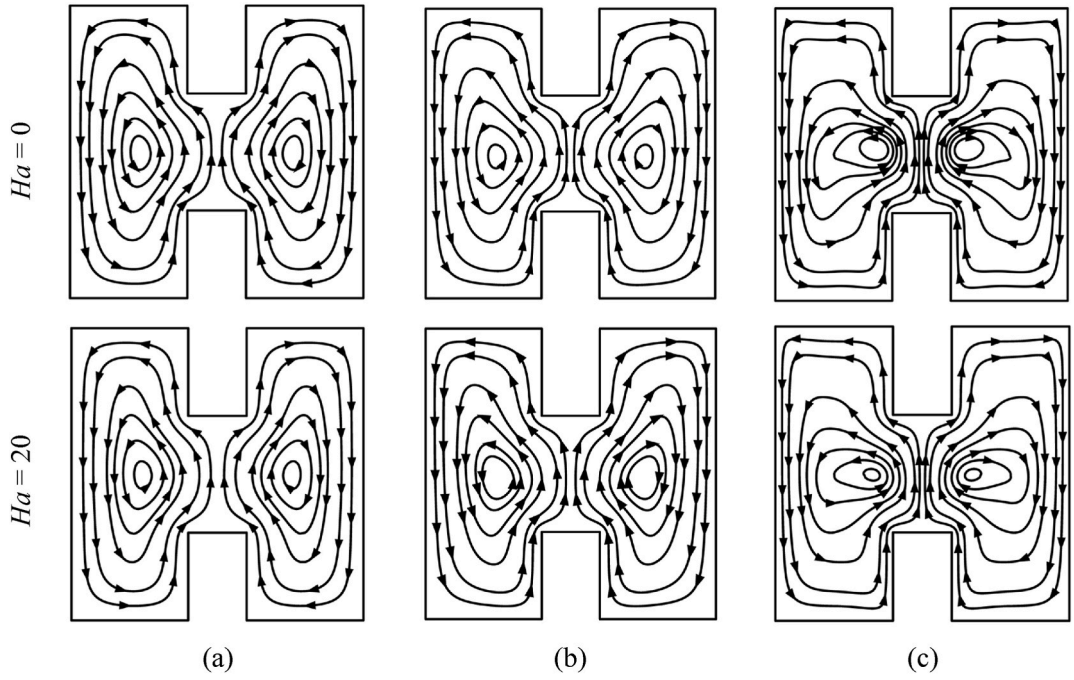

Fig. 8. Visualization of streamlines for $d/L = 0.4$ and $t/L = 0.4$ at (a) $Ra = 10^4$, (b) $Ra = 10^5$, and (c) $Ra = 10^6$ for different Hartmann numbers.

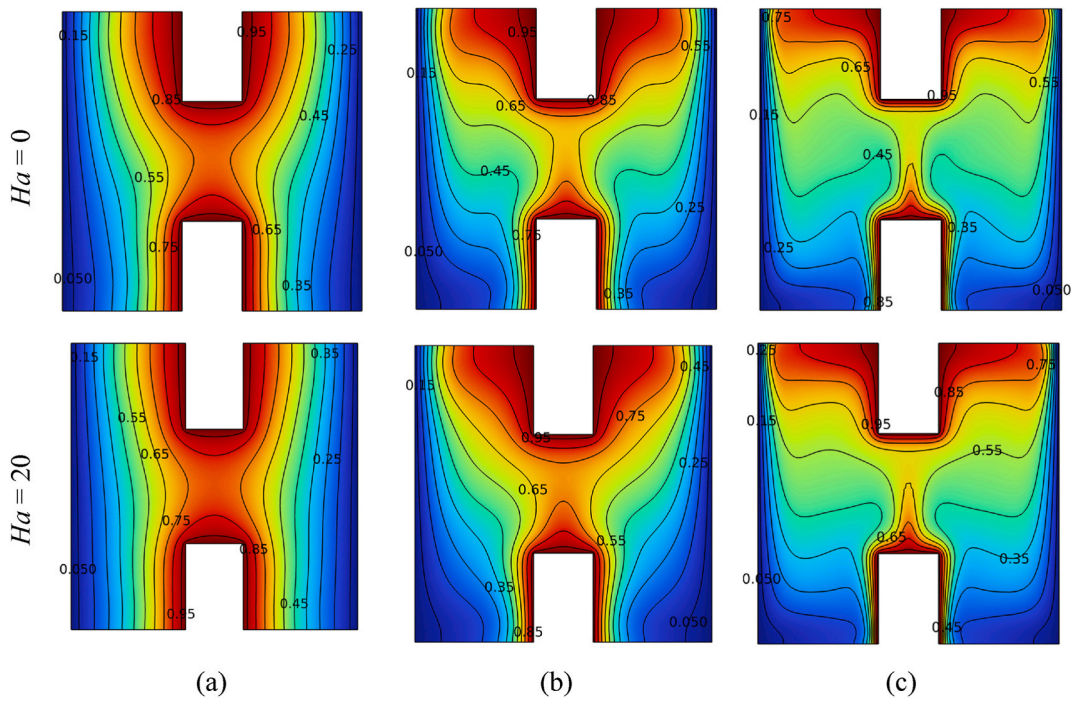

Fig. 9. Visualization of the iso-surface thermal field for $d/L = 0.4$ and $t/L = 0.4$ at (a) $Ra = 10^4$, (b) $Ra = 10^5$, and (c) $Ra = 10^6$ for different Hartmann numbers (color online). (For interpretation of the references to color in this figure legend, the reader is referred to the Web version of this article.)

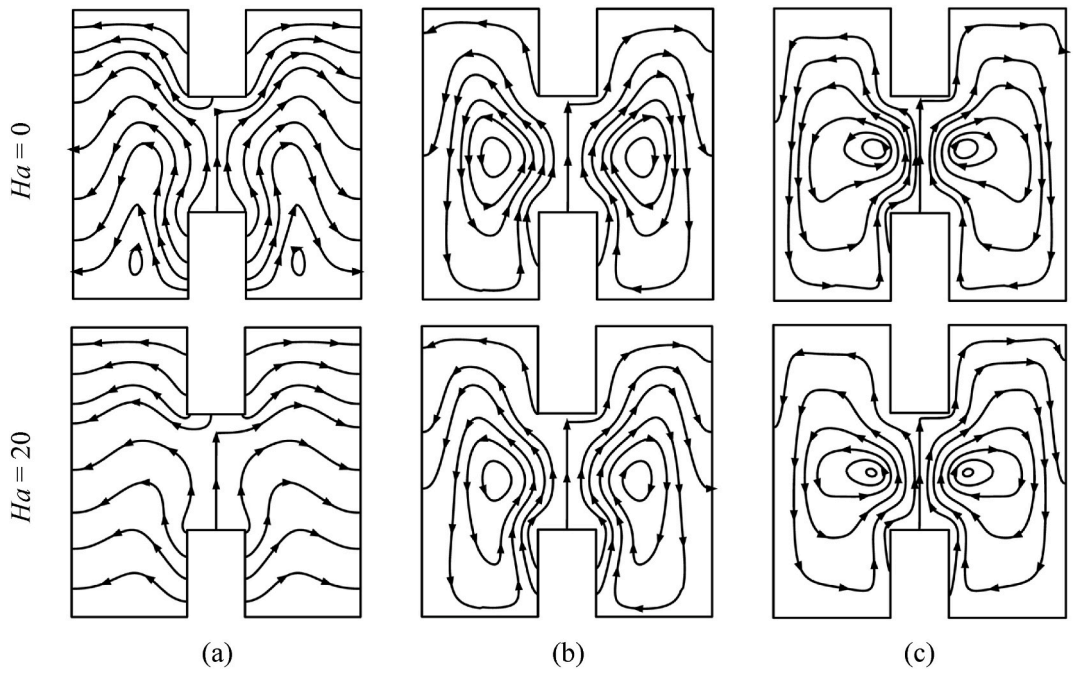

Fig. 10. Visualization of heatlines for $d/L = 0.4$ and $t/L = 0.4$ at (a) $Ra = 10^4$, (b) $Ra = 10^5$, and (c) $Ra = 10^6$ for different Hartmann numbers.

similar configurations as previously described. For a given Hartmann number, the behavior of the heatlines varies depending on the magnitudes of *Ra*. At lower Rayleigh numbers, the flow behavior is dominated by viscous forces, and heat transfer primarily occurs through conduction. Heatlines appear smooth and parallel, indicating a diffusion-dominated flow with limited fluid motion. In

addition, the flow pattern becomes almost horizontal, with no convective cells during the impact of the magnetic field ($Ha = 20$). When the Rayleigh number rises, buoyancy forces become more significant, contributing to fluid motion and heat transfer. Heatlines exhibit a more complex pattern with the generation of multiple convective cells. The induced chaotic fluid motion intensifies the generation of these vortices. The impact of the Hartmann number on heatline patterns can be interpreted at a low Rayleigh number (see Fig. 10(a)). Heatlines are generally affected by altering those of a non-magnetic system with parallel and smooth patterns. However, an increase in the Hartmann number at larger Rayleigh numbers leads to slight deviations in the heatline pattern due to the dominance of buoyancy forces. At higher Rayleigh numbers, buoyancy forces play a crucial role, and convection becomes the dominant mode of heat transfer. Even when the Hartmann number is high, the magnetic field's impact on the heat flow pattern is limited compared to the buoyancy forces. Heatlines display two convective cells characterizing Rayleigh-dominated flow, with the magnetic field exerting a secondary effect. The earlier results in Fig. 5(b) and (c) reveal similar findings as visually shown in Fig. 10.

5. Conclusion

The present investigation involves conducting numerical simulations to investigate the free convection phenomenon inside an *H*-shaped hollow structure or chamber filled with water, considering the impact of Joule heating and a magnetic field. The study examines MHD free convection features by varying both *Ra* and *Ha*, and the dimensions (width of the horizontal section and height of the middle section) of the chamber. The critical consequences of this investigation can be outlined as follows.

i. Augmenting *Ra* enhances convective heat transfer, resulting in higher *Nu*.
ii. Higher *Ra* and larger *t/L* ratios lead to better convective heat transfer, lower S_T and *TPC*.
iii. Mean fluid temperature decreases with increasing *Ra* and *Ha*. This effect becomes more pronounced at higher *Ra*.
iv. Increasing *Ha* suppresses fluid motion, reducing S_T and temperature gradients up to $Ra = 3 \times 10^3$. After that limit, thermal performance decreases with increasing *Ha*. The maximum reduction in *TPC* is 0.67 % for varying *Ha*.
v. For different *d/L* ratios, there are some shifting behaviors in *Nu* at $Ra = 4 \times 10^4$. Increasing *d/L* ratio from 0.2 to 0.4 decreases *TPC* for all values of *Ra* and *Ha*. The improvement in heat transfer performance is found to be maximum at $Ra = 2 \times 10^5$ by 87.8 %.
vi. Increasing the *t/L* ratio improves convective heat transfer, reduces S_T, and lowers *TPC*.

Anticipating future advancements, this study sets the stage for prospective research avenues in MHD free convection within *H*-shaped hollow structures. The findings pave the way for further exploring advanced control strategies and innovative materials to optimize thermal performance. To uncover additional insights, future investigations could delve into dynamic parameter variations, such as changing magnetic field direction. Integrating artificial intelligence and machine learning techniques for predictive modeling and control optimization could propel the field toward unprecedented efficiency and sustainability. Thus, this research addresses current knowledge gaps and acts as a catalyst for future breakthroughs in the dynamic realm of fluid mechanics and thermal engineering.

Data availability statement

Data will be made available on request.

CRediT authorship contribution statement

Md Hasibul Islam: Writing – review & editing, Writing – original draft, Visualization, Validation, Methodology, Investigation, Formal analysis, Data curation. **Riyan Hashem Jamy:** Writing – review & editing, Writing – original draft, Visualization, Validation, Methodology, Investigation, Formal analysis, Data curation. **Md Shahneoug Shuvo:** Writing – review & editing, Writing – original draft. **Sumon Saha:** Writing – review & editing, Writing – original draft, Supervision, Software, Formal analysis, Conceptualization, Data curation, Investigation, Methodology.

Declaration of competing interest

The authors declare that they have no known competing financial interests or personal relationships that could have appeared to influence the work reported in this paper.

Acknowledgments

The authors express their gratitude for the support from Basic Research Grant of BUET (grant no. 4747(45), SL.#9, dated April 13, 2022). They would also like to recognize the support of CFDHT Research Group at BUET for ensuring the necessary computational assistance throughout the investigation.

References

[1] S.R. Yan, S. Aghakhani, A. Karimipour, Influence of a membrane on nanofluid heat transfer and irreversibilities inside a cavity with two constant-temperature semicircular sources on the lower wall: applicable to solar collectors, Phys. Scripta 95 (8) (2020) 085702.

[2] Y. Zheng, S. Yaghoubi, A. Dezfulizadeh, S. Aghakhani, A. Karimipour, I. Tlili, Free convection/radiation and entropy generation analyses for nanofluid of inclined square enclosure with uniform magnetic field, J. Therm. Anal. Calorim. 141 (1) (2020) 635–648.

[3] A.H. Pordanjani, S. Aghakhani, Numerical investigation of natural convection and irreversibilities between two inclined concentric cylinders in presence of uniform magnetic field and radiation, Heat Tran. Eng. 43 (11) (2022) 937–957.

[4] G. De Vahl Davis, Natural convection of air in a square cavity: a bench mark numerical solution, Int. J. Numer. Methods Fluid. 3 (3) (1983) 249–264.

[5] M.M. Rahman, S. Mojumder, S. Saha, S. Mekhilef, R. Saidur, Augmentation of natural convection heat transfer in triangular shape solar collector by utilizing water based nanofluids having a corrugated bottom wall, Int. Commun. Heat Mass Tran. 50 (2014) 117–127.

[6] I. Chabani, F. Mebarek-Oudina, A.A.I. Ismail, MHD flow of a hybrid nanofluid in a triangular enclosure with zigzags and an elliptic obstacle, Micromachines 13 (2) (2022) 224.

[7] S. Mojumder, S. Saha, S. Saha, M.A. Mamun, Effect of magnetic field on natural convection in a *C*-shaped cavity filled with ferrofluid, Procedia Eng. 105 (2015) 96–104.

[8] S. Mojumder, K.M. Rabbi, S. Saha, M.N. Hasan, S.C. Saha, Magnetic field effect on natural convection and entropy generation in a half-moon shaped cavity with semi-circular bottom heater having different ferrofluid inside, J. Magn. Magn Mater. 407 (2016) 412–424.

[9] T. Tayebi, A.S. Dogonchi, A.J. Chamkha, M.B.B. Hamida, S. El-Sapa, A.M. Galal, Micropolar nanofluid thermal free convection and entropy generation through an inclined *I*-shaped enclosure with two hot cylinders, Case Stud. Therm. Eng. 31 (2022) 101813.

[10] T. Tayebi, S. El-Sapa, N. Karimi, A.S. Dogonchi, A.J. Chamkha, A.M. Galal, Double-diffusive natural convection with Soret/Dufour effects and energy optimization of Nano-Encapsulated Phase Change Material in a novel form of a wavy-walled *I*-shaped domain, J. Taiwan Inst. Chem. Eng. 148 (2023) 104873.

[11] R. Mohebbi, M. Izadi, H. Sajjadi, A.A. Delouei, M.A. Sheremet, Examining of nanofluid natural convection heat transfer in a *Γ*-shaped enclosure including a rectangular hot obstacle using the Lattice Boltzmann method, Phys. Stat. Mech. Appl. 526 (2019) 120831.

[12] Z.A. Raizah, S.E. Ahmed, A.M. Aly, ISPH simulations of natural convection flow in *E*-enclosure filled with a nanofluid including homogeneous/heterogeneous porous media and solid particles, Int. J. Heat Mass Tran. 160 (2020) 120153.

[13] H. Saleh, Z. Siri, M. Ghalambaz, Natural convection from a bottom heated of an asymmetrical *U*-shaped enclosure with nano-encapsulated phase change material, J. Energy Storage 38 (2021) 102538.

[14] M. Ferhi, R. Djebali, F. Mebarek-Oudina, N.H. Abu-Hamdeh, S. Abboudi, Magnetohydrodynamic free convection through entropy generation scrutiny of eco-friendly nanoliquid in a divided *L*-shaped heat exchanger with Lattice Boltzmann method simulation, Journal of Nanofluids 11 (1) (2022) 99–112.

[15] R.H. Jamy, S. Chowdhury, F.K. Chowdhury, S. Saha, Analyzing overall thermal behaviour of conjugate MHD free convection in *L*-shaped chamber with a thick fin, Case Stud. Therm. Eng. 48 (2023) 103137.

[16] M.A. Mansour, S.E. Ahmed, M.A. Bakier, Free convection in *H*-shaped enclosures filled with a porous medium saturated with nanofluids with mounted heaters on the vertical walls, Special Topics and Reviews in Porous Media, Int. J. 4 (2013) 287–297.

[17] A. Rahimi, M. Sepehr, M.J. Lariche, M. Mesbah, A. Kasaeipoor, E.H. Malekshah, Analysis of natural convection in nanofluid-filled *H*-shaped cavity by entropy generation and heatline visualization using Lattice Boltzmann method, Phys. E Low-dimens. Syst. Nanostruct. 97 (2018) 347–362.

[18] F. Keramat, P. Dehghan, M. Mofarahi, C.H. Lee, Numerical analysis of natural convection of alumina–water nanofluid in *H*-shaped enclosure with a *V*-shaped baffle, J. Taiwan Inst. Chem. Eng. 111 (2020) 63–72.

[19] F. Keramat, A. Azari, H. Rahideh, M. Abbasi, A CFD parametric analysis of natural convection in an *H*-shaped cavity with two-sided inclined porous fins, J. Taiwan Inst. Chem. Eng. 114 (2020) 142–152.

[20] M. Loukili, K. Kotrasova, D. Dutykh, A computational simulation of steady natural convection in an *H*-form cavity, Software Engineering Perspectives in Intelligent Systems: Proceedings of 4th Computational Methods in Systems and Software 2 (2020) 164–177.

[21] Z.A. Raizah, A.M. Aly, Natural convection in an *H*-shaped porous enclosure filled with a nanofluid, Comput. Mater. Continua (CMC) 66 (3) (2021) 3233–3251.

[22] Z. Yuan, Y. Dong, Z. Jin, Numerical simulation of MHD natural convection and entropy generation in semicircular cavity based on LBM, Energies 16 (10) (2023) 4055.

[23] E. Sourtiji, S.F. Hosseinizadeh, Heat transfer augmentation of magnetohydrodynamics natural convection in *L*-shaped cavities utilizing nanofluids, Therm. Sci. 16 (2) (2012) 489–501.

[24] P.X. Yu, J.X. Qiu, Q. Qin, Z.F. Tian, Numerical investigation of natural convection in a rectangular cavity under different directions of uniform magnetic field, Int. J. Heat Mass Tran. 67 (2013) 1131–1144.

[25] I.D. Azzawi, A. Al-damook, The optimum computational simulation of MHD natural convection for improved cooling efficiency and entropy performance inside *M*-shaped cabinet, Numer. Heat Tran., Part A: Applications (2023) 1–20.

[26] I. Rahmoune, S. Bougoul, MHD natural convection in a cavity partially heated having a wavy wall and filled with Al_2O_3-water nanofluid, Algerian Journal of Engineering and Technology 8 (1) (2023) 84–93.

[27] O. Ghaffarpasand, Conjugate effect of Joule heating and unsteady MHD natural convection in a differentially heated skewed porous cavity saturated by Cu-water nanofluid, J. Appl. Fluid Mech. 9 (6) (2016) 2823–2836.

[28] B. Vasu, MHD free convection flow of power-law nanofluid film along an inclined surface with viscous dissipation and Joule heating, World J. Eng. 16 (1) (2019) 115–124.

[29] M. Gholinia, M.E. Hoseini, S. Gholinia, A numerical investigation of free convection MHD flow of Walters-B nanofluid over an inclined stretching sheet under the impact of Joule heating, Therm. Sci. Eng. Prog. 11 (2019) 272–282.

[30] S. Tasnim, A. Mitra, H. Saha, M.Q. Islam, S. Saha, MHD conjugate natural convection and entropy generation of a nanofluid filled square enclosure with multiple heat-generating elements in the presence of Joule heating, Results in Engineering 17 (2023) 100993.

[31] F. Selimefendigil, H.F. Öztop, N. Abu-Hamdeh, Natural convection and entropy generation in nanofluid filled entrapped trapezoidal cavities under the influence of magnetic field, Entropy 18 (2) (2016) 43.

[32] Z. Li, A.K. Hussein, O. Younis, M. Afrand, S. Feng, Natural convection and entropy generation of a nanofluid around a circular baffle inside an inclined square cavity under thermal radiation and magnetic field effects, Int. Commun. Heat Mass Tran. 116 (2020) 104650.

[33] T. Tayebi, A.J. Chamkha, MHD buoyancy-driven flow in a nanoliquid filled-square enclosure divided by a solid conductive wall, Math. Methods Appl. Sci. (2020) 1–17.

[34] Y. Khetib, A.A. Alahmadi, A. Alzaed, A. Tahmasebi, M. Sharifpur, G. Cheraghian, Natural convection and entropy generation of MgO/water nanofluids in the enclosure under a magnetic field and radiation effects, Processes 9 (8) (2021) 1277.

[35] H. Cheng, S.M. Sajadi, M.Z. Jouzdani, Control of hybrid nanofluid natural convection with entropy generation: a LBM analysis based on the irreversibility of thermodynamic laws, Eng. Anal. Bound. Elem. 155 (2023) 108–120.

[36] F. Mebarek-Oudina, I. Chabani, H. Vaidya, A.A. Ismail, Hybrid-nanofluid magneto-convective flow and porous media contribution to entropy generation, Int. J. Numer. Methods Heat Fluid Flow 34 (2) (2024) 809–836.

[37] Y.A. Cengel, A.J. Ghajar, Heat and Mass Transfer: Fundamentals and Applications, sixth ed., McGraw-Hill Education, New York, 2020.

[38] S. Javed, N. Deb, S. Saha, Natural convection and entropy generation inside a square chamber divided by a corrugated porous partition, Results in Engineering 18 (2023) 101053.

[39] H.T. Zisan, T.H. Ruvo, S. Saha, Entropy generation and natural convection on a cubic cavity with a pair of heat source at different configurations, Int. Commun. Heat Mass Tran. 134 (2022) 106033.

[40] T.H. Ruvo, H.T. Zisan, S. Saha, Analysis of conjugate Marangoni natural convection in a heating system with an open boundary flow, Int. Commun. Heat Mass Tran. 138 (2022) 106402.

[41] M.S. Shuvo, F. Ishtiaq, T. Jamee, J. Das, S. Saha, Analysis of internal cooling system in a vented cavity using P, PI, PID controllers, Results in Engineering 15 (2022) 100579.
[42] S. Javed, S. Saha, Estimation of comprehensive thermal performance for conjugate natural convection inside a dome-shaped porous chamber holding a solid cylinder, Results in Engineering 18 (2023) 100896.
[43] M.S. Shuvo, M.M. Ikram, M.N. Hasan, S. Saha, Thermal resistance analysis on conjugate free convective flow in a thick-walled square chamber, Case Stud. Therm. Eng. 51 (2023) 103644.
[44] F. Corvaro, M. Paroncini, An experimental study of natural convection in a differentially heated cavity through a 2D-PIV system, Int. J. Heat Mass Tran. 52 (1–2) (2009) 355–365.

Nomenclature

a: Surface area (m^2)
B_0: Magnetic field strength (T)
C_p: Specific heat capacity (J/kg.K)
d: Width of the vertical section (m)
g: Gravitational acceleration (m/s^2)
H: Dimensionless heat function
Ha: Hartmann number
J: Joule heating parameter
k: Thermal conductivity of water (W/m.K)
L: Reference length of the structure (m)
N: Dimensionless wall-normal distance
n: Wall-normal distance (m)
N_E: Number of mesh elements
Nu: Mean Nusselt number
P: Dimensionless pressure
p: Pressure (Pa)
Pr: Prandtl number
Ra: Rayleigh number
S: Dimensionless surface length, dimensionless local entropy generation
s: Surface length (m), local entropy generation (W/m^3K)
T: Temperature (K)
t: Thickness of the horizontal middle section (m)
u, v: Velocity components (m/s)
U, V: Dimensionless velocity components
x, y: Cartesian coordinates (m)
X, Y: Dimensionless Cartesian coordinates

Greek Symbols

α: Thermal diffusivity (m^2/s)
Θ: Dimensionless temperature
σ: Electrical conductivity (S/m)
φ: Irreversibility coefficient
Ψ: Dimensionless stream function
β: Volumetric thermal expansion coefficient (1/K)
μ: Dynamic viscosity (Pa.s)
ρ: Mass density (kg/m^3)

Subscripts

av: average
c: cold
e: each heated surface
ff: fluid friction
h: hot
ht: heat transfer
m: mean
mf: magnetic field
ref: reference
s: individual surface
T: total

Abbreviations

CFD: Computational fluid dynamics
MHD: Magnetohydrodynamic
PCB: Printed circuit board
TPC: Thermal performance criterion